BIOCHEMISTRY

Relaxed initiation pausing of ribosomes drives oncogenic translation

Leiming Dong[1]*, Yuanhui Mao[1]*, Aidong Zhou[2], Xiao-Min Liu[1†], Jun Zhou[1†], Ji Wan[1], Shu-Bing Qian[1‡]

Translation is a crucial process in cancer development and progression. Many oncogenic signaling pathways target the translation initiation stage to satisfy the increased anabolic demands of cancer cells. Using quantitative profiling of initiating ribosomes, we found that ribosomal pausing at the start codon serves as a "brake" to restrain the translational output. In response to oncogenic RAS signaling, the initiation pausing relaxes and contributes to the increased translational flux. Intriguingly, messenger RNA (mRNA) m^{6}A modification in the vicinity of start codons influences the behavior of initiating ribosomes. Under oncogenic RAS signaling, the reduced mRNA methylation leads to relaxed initiation pausing, thereby promoting malignant transformation and tumor growth. Restored initiation pausing by inhibiting m^{6}A demethylases suppresses RAS-mediated oncogenic translation and subsequent tumorigenesis. Our findings unveil a paradigm of translational control that is co-opted by RAS mutant cancer cells to drive malignant phenotypes.

INTRODUCTION

Dysregulation of mRNA translation is a frequent feature of cancer cells (*1*–*3*). Many oncogenic signaling pathways (e.g., RAS, phosphatidylinositol 3-kinase/mechanistic target of rapamycin (mTOR), and MYC) converge to regulate the assembly and activity of eIF4F, a protein complex responsible for ribosome loading to the 5′ end cap of mRNAs (*4*–*6*). By controlling the translational efficiency of specific messages, eIF4F serves as a critical nexus for cancer development (*7*). As a result, malignant cells often become "addicted" to elevated protein synthesis. Over the past several years, there has been much effort to target translation initiation in cancer treatment. However, recent clinical trials using inhibitors targeting eIF4F or its upstream regulators (e.g., mTOR) showed only limited efficacy (*8*). It is possible that the mechanistic linkage between dysregulated translation initiation and tumorigenesis is more complex than previously thought.

Eukaryotic translation initiation typically begins with the recruitment of a 40*S* ribosome subunit to the 5′ end cap of an mRNA. In complex with initiation factors, the ribosome then scans along the 5′ untranslated region (5′UTR) until an initiation codon is encountered. Successful engagement of the scanning ribosome to a start codon is marked by the joining of a 60*S* subunit. It is generally believed that, once the 80*S* ribosome is assembled at the start codon, elongation proceeds to begin polypeptide synthesis. Much attention has been focused on the events involving ribosome loading, scanning, and start codon selection (*9*). Very little is known about the ribosome dynamics at start codons before the commitment of polypeptide synthesis.

Recent studies point to a role for the mRNA methylation program in translational regulation and cancer biology. In mammalian cells, the most abundant internal mRNA modification is N^6-methyladenosine (m^{6}A) (*10*). The dynamic m^{6}A modification is achieved by two opposing enzyme systems: the methyltransferase complex comprising a core heterodimer of METTL3-METTL14, and m^{6}A demethylases FTO and ALKBH5. The YTH domain family proteins serve as the major m^{6}A-binding proteins to regulate nearly all aspects of mRNA metabolism and functionality. While we start to appreciate the importance of epitranscriptome in a diverse array of cellular processes, the overall impact of mRNA methylation in cancer biology is complex. Depending on cell types, loss of m^{6}A has been shown to yield different outcomes. For instance, elevated levels of ALKBH5 and subsequent m^{6}A depletion have been shown to drive hypoxia-associated cancer stem cell formation in breast cancer (*11*). In glioblastoma and endometrial cancer models, depleting m^{6}A-promoted tumorigenesis, arguing a tumor suppressor role for METTL3 (*12*–*15*). However, the opposite holds true in different types of cancer. For instance, METTL3 seems to promote lung cancer cell growth, at least in culture (*16*). A recent study reported that overexpression of METTL3 increases proliferation of acute myeloid leukemia (AML) cells (*17*). These perplexing results challenge the rational design of therapeutic strategies targeting mRNA methylation in different cancers. There is a pressing need to understand in greater detail the mechanistic connection between m^{6}A modification and cancer-relevant processes.

The small guanosine triphosphatase (GTPase) RAS is frequently mutated in human malignancies (*18*, *19*). In pancreatic cancer, mutations in KRAS are found in more than 90% of patient samples. Mouse studies have provided compelling evidence that oncogenic RAS is required for both initiation and maintenance of pancreatic cancer (*20*). Despite more than three decades of research effort, clinically effective anti-RAS therapies have remained elusive. In search for the signature of RAS^{G12V}-mediated oncogenic translation, we found an unexpected checkpoint between initiation and elongation. Intriguingly, the start codon–associated ribosome pausing is influenced by mRNA methylation in the form of m^{6}A. We demonstrate that the tight coordination between eIF4F-mediated cap recognition and start codon–associated ribosome pausing fine-tunes the translational flux, which is co-opted by mutant RAS cancer cells to satisfy their increased anabolic demands. To explore the therapeutic potential of restoring initiation pausing, we took advantage

[1]Division of Nutritional Sciences, Cornell University, Ithaca, NY 14853, USA. [2]Department of Cell Biology, Southern Medical University, Guangzhou 510515, China.
*These authors contributed equally to this work.
†Present address: School of Life Science and Technology, China Pharmaceutical University, Nanjing 211198, China.
‡Corresponding author. Email: sq38@cornell.edu

of a small-molecule inhibitor of m^{6}A demethylase FTO, which exhibits remarkable anti-tumorigenesis toward mutant RAS cancers.

RESULTS

RAS^{G12V}-mediated oncogenic translation

Cancer-causing RAS mutations impair the GTPase activity, resulting in constitutive activation of the RAS signaling pathway. Since the oncogenic potential of RAS often manifests in a context-dependent manner, the translational status associated with malignant progression is confounded by mixed genetic backgrounds and varying tissue environments. To circumvent this complexity, we took advantage of a human TtH cell line stably expressing a 4-hydroxytamoxifen (4-OHT)–inducible ER:HRAS^{G12V} fusion protein (*21*). This system permits direct comparison of translational landscapes with or without oncogenic RAS expression under the same genetic background. Upon treatment with 4-OHT, ER:HRAS^{G12V} was readily detectable in these cells (Fig. 1A) but not the vector control cells (fig. S1A). As expected, oncogenic RAS expression led to increased phosphorylation of Akt as well as mTOR complex 1 (mTORC1) downstream targets S6K1 and 4EBP1 (Fig. 1A). 4-OHT treatment increased the polysome/monosome (P/M) ratio (Fig. 1B), confirming that hyperactive RAS signaling stimulates protein synthesis (*4*, *21*). In agreement, a firefly luciferase (Fluc) reporter also showed an increased expression in the presence of 4-OHT (Fig. 1C). The enhanced translational capacity was not due to the side effect of 4-OHT because the same treatment had negligible effect in vector control cells (fig. S1, B and C).

It is unclear whether the increased translational output in the presence of RAS^{G12V} is the sole consequence of augmented mTORC1 signaling. If so, then mTORC1 inhibition is expected to eliminate the translational difference between cells with or without oncogenic RAS expression. We examined the effect of Torin1, a potent active site mTOR inhibitor (*22*). As expected, Torin1 treatment caused a rapid dephosphorylation of S6K1 and 4EBP1 (Fig. 1A). Although the overall translation was reduced in the presence of Torin1, as evidenced by the disassembly of polysomes, cells with RAS^{G12V} expression still exhibited a relatively higher P/M ratio than control cells (Fig. 1B). The sustained translational up-regulation caused by RAS^{G12V} expression was also seen in the Fluc reporter assay (Fig. 1C). As an independent validation, we examined the synthesis of endogenous proteins using puromycin labeling. The total levels of puromycin-labeled nascent chains were increased after 4-OHT treatment (Fig. 1D), confirming the enhanced synthesis of endogenous proteins during oncogenic translation. However, despite the dose-dependent inhibition by Torin1, translation nevertheless remained high in cells expressing RAS^{G12V} even in the presence of a high dose of Torin1 (100 nM) (Fig. 1D). The similar finding was obtained from [^{35}S] metabolic labeling (fig. S1D). These results suggest that additional mechanisms may contribute to RAS^{G12V}-mediated oncogenic translation.

Relaxed initiation pausing during oncogenic translation

To illustrate a holistic view of RAS^{G12V}-stimulated translation, we conducted RNA sequencing (RNA-seq), ribosome profiling (Ribo-seq), and quantitative translation initiation sequencing (QTI-seq) in TtH cells before and after 4-OHT treatment (Fig. 2A). Ribo-seq measures the density of ribosome footprints across the coding region (CDS) (*23*, *24*). By normalizing to the mRNA abundance, the averaged ribosome occupancy often serves as a proxy for translation efficiency. However, RAS^{G12V} expression altered global protein synthesis with little mRNA specificity (Fig. 2B, middle, and Fig. 2C, right). Unlike Ribo-seq, QTI-seq captures initiating ribosomes in a quantitative manner and permits global mapping of translation initiation sites (TIS) and measurement of the ribosome density at individual start codons (*25*). To our surprise, most of start codons showed reduced or disappeared ribosome density upon RAS^{G12V} expression (Fig. 2C, left). The reduced ribosome density at the annotated TIS (aTIS) in the presence of 4-OHT could not be ascribed to inhibited translation initiation because Ribo-seq revealed no evident decrease of footprints in CDS (Fig. 2C, right). Certain transcripts even showed an increased CDS occupancy as exemplified by *RPS19* (Fig. 2D) and EEF1G (fig. S2A). While the aTIS density of *RPS19* dropped >10-fold after 4-OHT treatment, its CDS occupancy was increased by 2.5-fold. We reasoned that, during oncogenic translation, the initiating ribosome undergoes faster commitment

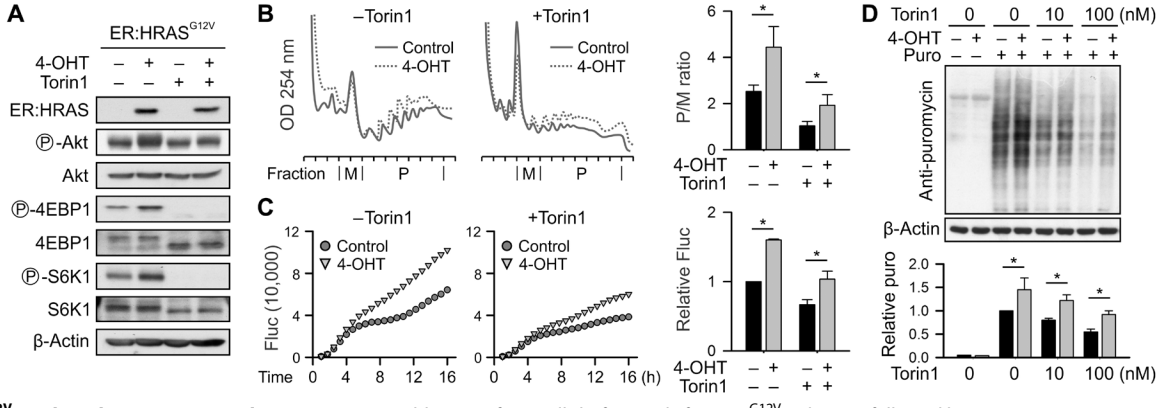

Fig. 1. RAS^{G12V}-mediated oncogenic translation. (**A**) Western blotting of TtH cells before and after RAS^{G12V} induction followed by Torin1 treatment (50 nM for 2 hours). Activation of mTORC1 downstream targets was evaluated by their phosphorylation status. (**B**) Polysome profiles of TtH cells before and after RAS^{G12V} induction, with and without Torin1 treatment. M, monosome; P, polysome. The right panel shows the P/M ratio calculated using areas below the curve. OD, optical density. (**C**) Real-time Fluc reporter assay in TtH cells before and after RAS^{G12V} induction, with and without Torin1 treatment (50 nM). The right panel shows the relative Fluc levels at 15 hours post-transfection after normalization with mRNA levels. (**D**) Puromycin labeling assay in TtH cells before and after RAS^{G12V} induction followed by 2 hours of Torin1 treatment with different doses. The bottom panel shows the relative levels of puromycin-labeled nascent chains quantified by densitometry. Error bars, means ± SEM; *$P < 0.05$, unpaired two tailed *t* test; $n = 3$ biological replicates (from B to D).

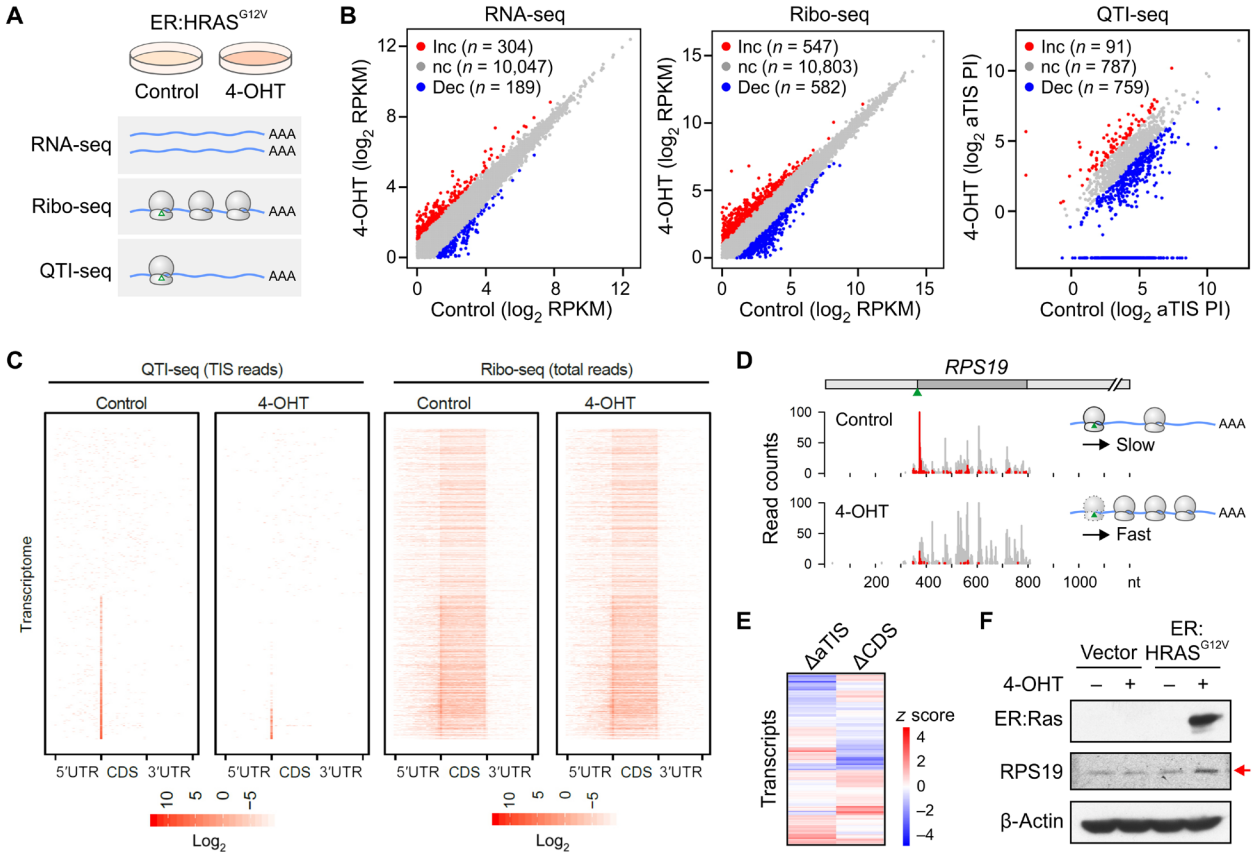

Fig. 2. RAS^{G12V}-mediated oncogenic translation involves relaxed initiation pausing of ribosomes. (**A**) Schematic of RNA-seq, Ribo-seq, and QTI-seq analysis using TtH cells before and after RAS^{G12V} induction. (**B**) Scatter plots of individual transcripts in TtH cells with and without RAS^{G12V} induction. Log_2 values of reads per kilobase of transcript per million mapped reads (RPKM) are used for RNA-seq and Ribo-seq comparison. Annotated translation initiation site (aTIS) pausing index (PI) is computed as the ratio of aTIS mean density at the annotated start codon window (±5 nt) over the CDS background captured by QTI-seq. Transcripts with different fold changes after 4-OHT treatment are color-coded. (**C**) Heatmaps showing the density of TIS peaks (left) and ribosome occupancy (right) in ER:HRAS^{G12V} cells before and after 4-OHT treatment. TIS peaks are identified from putative open reading frames derived from QTI-seq. (**D**) A transcript example (*RPS19*) exhibiting a decrease of aTIS PI upon RAS^{G12V} induction. Color-coded are reads from Ribo-seq (gray) and QTI-seq (red). (**E**) Heatmap depicting fold changes of aTIS PI (ΔaTIS) and CDS ribosome occupancy (ΔCDS) upon RAS^{G12V} induction. (**F**) Immunoblotting of endogenous proteins in ER:HRAS^{G12V} cells before and after 4-OHT treatment.

to elongation at the start codon. Hence, QTI-seq is less likely to capture these initiating ribosomes. We are particularly attracted to this possibility, as it would suggest that a faster transition from initiation to elongation increases the translational output under oncogenic RAS signaling.

The ribosome density at the start codon reflects how long an initiating ribosome resides at the main start codon before the elongation commitment. However, it could be influenced by different initiation rates (i.e., the ribosome loading efficiency) and mRNA abundance. To factor out these variations, we divided the total reads at the annotated start codon (aTIS) by the mean background reads in CDS captured by QTI-seq. The resultant aTIS pausing index (PI) represents, on a relative scale, the dwell time of initiating ribosomes at individual start codons. The similar approach was originally designed to compute promoter-proximal pausing of RNA polymerase II (*26*). As shown in Fig. 2B, nearly half of the transcripts showed decreased aTIS PI (>2-fold) upon RAS^{G12V} expression. The lowered aTIS density under oncogenic RAS signaling is highly reproducible in biological replicates (fig. S2B). In comparison to Ribo-seq, a substantial amount of transcripts experiencing reduced aTIS PI after 4-OHT treatment exhibited increased ribosome occupancy in CDS (Fig. 2E). In line with the increased translation yield, immunoblotting showed elevated protein levels of RPS19 in cells after 4-OHT treatment (Fig. 2F). Therefore, oncogenic RAS signaling is accompanied with relaxed initiation pausing that results in an increased translational output.

Characterizing ribosome initiation pausing

The unexpected "lingering" of an 80*S* ribosome at the start codon before productive elongation suggests a previously unappreciated mechanism by which initiation pausing regulates translation efficiency, at least for some transcripts. It is conceivable that, under the physiological condition, initiation pausing limits the translational output by acting as a barrier for productive elongation (fig. S2C). Supporting this notion, a negative correlation ($R = -0.22$) was evident between the aTIS PI and the CDS ribosome occupancy (Fig. 3A). This salient feature is highly reproducible in biological replicates, in different cell types, and in mouse liver samples (fig. S2D). Therefore, initiation pausing represents an inherent feature for individual transcripts. We searched for common biological themes among

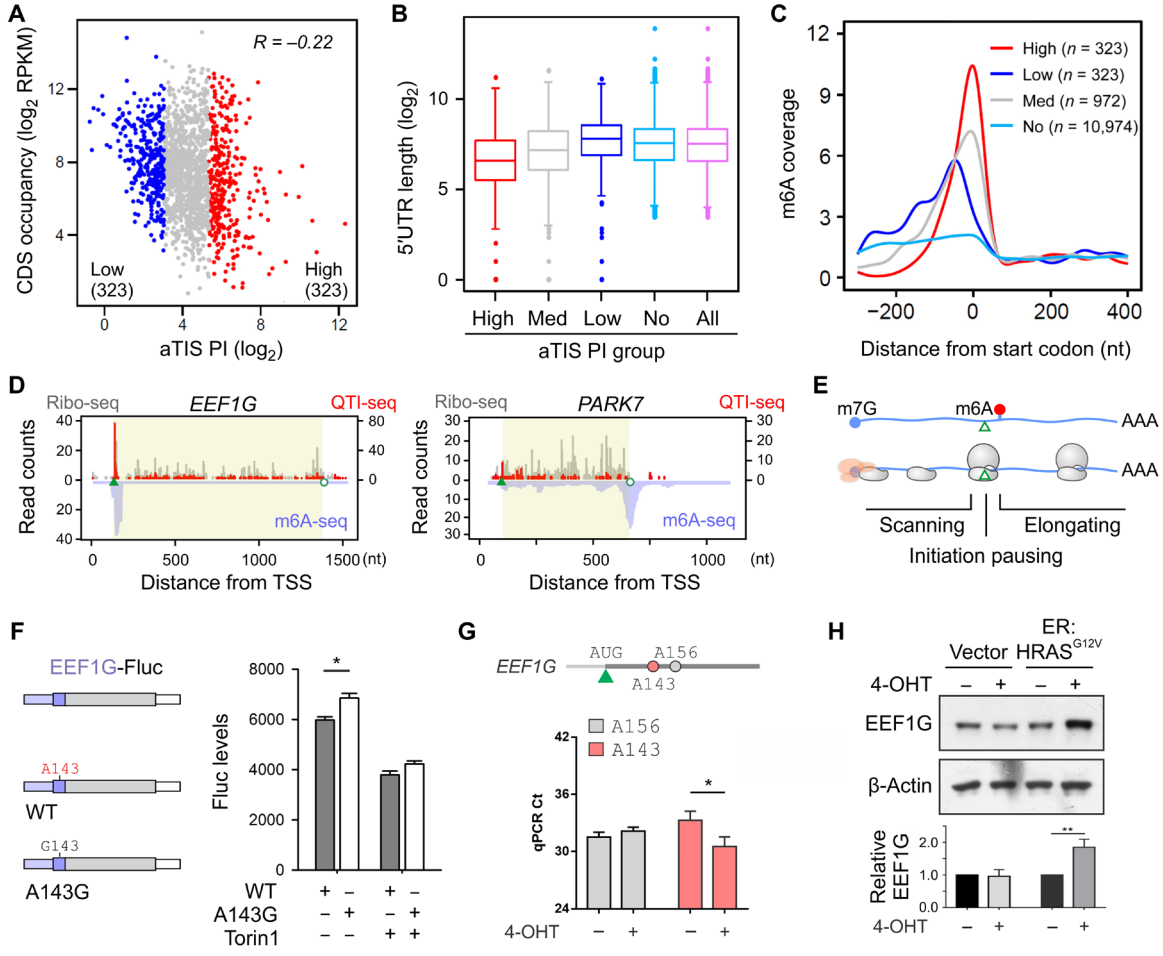

Fig. 3. Initiation pausing of ribosomes is regulated by mRNA methylation. (**A**) A scatter plot shows the negative correlation between the aTIS PI and the CDS ribosome occupancy of individual transcripts. (**B**) A box plot shows the distribution of 5′UTR length for transcripts stratified on the basis of aTIS PI. (**C**) Metagene profiles of m^{6}A coverage around start codons of the transcripts stratified on the basis of aTIS PI values. (**D**) Examples of transcripts with high (*EEF1G*) and low (*PARK7*) values of aTIS PI. Color-coded are reads from Ribo-seq (gray), QTI-seq (red), and m^{6}A-seq (light blue). TSS, transcription start site. (**E**) A schematic diagram depicts the initiation pausing of ribosomes during the transition from initiation to elongation. (**F**) Fluc reporter assays using *EEF1G* 5′UTR with or without A143G mutant in transfected HEK293 cells in the absence or presence of Torin1. WT, wild type. (**G**) SELECT measurement of m^{6}A levels on *EEF1G* mRNA in TtH cells with or without 4-OHT treatment. qPCR, quantitative polymerase chain reaction. (**H**) Western blots of endogenous EEF1G in TtH cells with or without 4-OHT treatment. The bottom panel shows the quantification of EEF1G. Error bars, means ± SEM; $^*P < 0.05$, $^{**}P < 0.01$, unpaired two tailed *t* test; $n = 3$ biological replicates (from F to H).

transcripts with relatively high aTIS PI using gene ontology (GO) analysis. Genes involved in cell growth and proliferation, such as translation and cell cycle, were overrepresented among mRNAs exhibiting strong initiation pausing (fig. S2E). Pathway analysis also revealed the same functional category for transcripts with high aTIS PI values (fig. S2F).

An immediate outstanding question is what, if any, sequence features could contribute to varied ribosome pausing during the transition from initiation to elongation. We first examined the structural features of mRNAs with high or low aTIS PI. However, mRNA regions surrounding the start codon (−100 to +300 nt) exhibited comparable thermal dynamic stability between transcripts with or without initiation pausing (fig. S3A). This was further corroborated by the similar secondary structures determined experimentally via either parallel analysis of RNA structures (PARS) score measurement or dimethyl sulfate sequencing (DMS-seq) (*27*, *28*) (fig. S3, B and C). We found that transcripts with shorter 5′UTR length tend to have higher aTIS PI values (Fig. 3B). Since longer 5′UTR can accommodate multiple scanning ribosomes, it is possible that a direct "push" by subsequent ribosomes helps release initiation pausing. However, the static mRNA sequence feature unlikely explains the altered aTIS PI in response to oncogenic RAS signaling. We hypothesize that additional regulatory factors must be at play to influence the behavior of scanning ribosomes at the start codon.

5′UTR methylation regulates initiation pausing

We recently reported that the scanning process of translation initiation is subjected to regulation by 5′UTR methylation in the form of m^{6}A (*29*). To illustrate the m^{6}A topology for mRNAs undergoing active translation, we collected ribosome-associated mRNAs followed by m^{6}A sequencing (m^{6}A-seq). On a transcriptome-wide scale, we observed an expected landscape of methylation with m^{6}A sites highly enriched around the stop codon (fig. S3D). To our surprise, transcripts with high aTIS PI exhibited a marked enrichment of m^{6}A in the vicinity of start codon with the peak density of >4-fold

higher above the average (Fig. 3C). For example, in TtH cells, *EEF1G* bears methylation only near the start codon region and consequently displayed a prominent initiation pausing (Fig. 3D). By contrast, *PARK7* is primarily methylated around the stop codon and shows minimal aTIS peak. Notably, in human embryonic kidney (HEK) 293 cells, *PARK7* shows two m^{6}A peaks in the vicinity of both start and stop codons. As a result, the initiation pausing becomes evident (fig. S3E). Therefore, despite the cell type–specific variations of m^{6}A, there is a strong correlation between initiation pausing and start codon–associated m^{6}A. Intriguingly, nearly half of the transcripts showed no identifiable TIS sites, although some of these messages were abundant and highly translated (Fig. 2C). We found that this group of mRNAs bears the lowest m^{6}A levels in the vicinity of start codons (Fig. 3C). The distinct m^{6}A enrichment near the start codon of transcripts with differential aTIS PI also holds true in other cell types including mouse liver tissues (fig. S3D). The antibody-based m^{6}A-seq might have limitations (*30*). We queried recent m^{6}A datasets using antibody-free mapping approach, such as deamination adjacent to RNA modification targets (DART-seq) (*31*), m^{6}A-SEAL (*32*), and m^{6}A-label-seq (*33*). Despite considerable variation, m^{6}A around the start codon exhibits higher levels for mRNAs with aTIS peaks (fig. S3F). These results collectively suggest a functional correlation between start codon–associated m^{6}A modification and initiation pausing (Fig. 3E).

To independently test this hypothesis, we created reporters by fusing the first 200 nt of *EEFIG* containing the full-length 5′UTR and the first 54 nt of CDS to the Fluc and introduced A→G mutation into the m^{6}A site (A143). In transfected cells, the A143G mutant exhibited higher Fluc levels than the wild-type reporter (Fig. 3F). To examine the behavior of endogenous EEF1G, we used single-base elongation- and ligation-based qPCR amplification method (SELECT) to quantify the site-specific m^{6}A levels. SELECT is a sensitive method based on the ability of m^{6}A to hinder the single-base elongation activity of DNA polymerases and the nick ligation efficiency of ligases (*34*). In TtH cells, 4-OHT treatment resulted in reduced m^{6}A levels at A143 (Fig. 3G). As a negative control, the neighboring A156 showed little difference. We then examined the protein levels of endogenous EEF1G and found an evident increase of EEF1G upon oncogenic RAS signaling (Fig. 3H). These results collectively support the notion that m^{6}A modification in the start codon vicinity restricts the translational output.

Reduced mRNA methylation in cancers with RAS mutations

To investigate whether the relaxed initiation pausing during oncogenic translation is a result of reduced mRNA methylation, we purified poly(A)$^+$ RNAs from cells with or without RAS^{G12V} expression followed by m^{6}A dot blotting. In cells treated with 4-OHT, we found approximately 40% reduction of total mRNA m^{6}A levels (Fig. 4A). This was not due to the side effect of 4-OHT because the same treatment did not alter m^{6}A levels in vector control cells (fig. S4A). The lowered methylation upon oncogenic RAS signaling was further confirmed by a commercial m^{6}A quantification kit (fig. S4B). We next measured m^{6}A methyltransferase and demethylase activities in these cells. While 4-OHT treatment had little effect on the demethylase activity, we observed a 43% reduction of the methyltransferase activity in cells expressing ER:RAS^{G12V} (Fig. 4B). To probe the mechanism by which oncogenic RAS signaling reduces mRNA methylation, we examined the integrity of the m^{6}A machinery via immunoprecipitation (IP). Despite the similar steady-state levels, METTL3 exhibited decreased association with Wilms' tumor 1-associating protein (WTAP) in cells with oncogenic RAS signaling (Fig. 4C). Transcriptome-wide m^{6}A-seq revealed a similar topology of m^{6}A distribution before and after 4-OHT treatment, suggesting that oncogenic RAS signaling is associated with a global reduction of mRNA methylation (fig. S4C).

The role of METTL3 in tumorigenesis is complex as different phenotypes have been observed from different types of cancers. From The Cancer Genome Atlas database, recurrent missense mutations of METTL3 and METTL14 have been identified in several types of human cancers, in particular pancreatic and endometrial cancers (Fig. 4D). The most commonly mutated sites are within the conserved methyltransferase domain MT-A70. The mutant form of METTL14 shows reduced methyltransferase activity (*35*). This finding strongly suggests a tumor suppressor role for m^{6}A methyltransferase, at least in certain types of cancers. Furthermore, Kaplan-Meier plotter revealed that high expression of METTL3 correlates with increased overall survival of patients with pancreatic cancer but not liver cancers (Fig. 4E). Since more than 90% of pancreatic cancers bear RAS mutations (*19*), the cancer type–specific clinical correlation between METTL3 and patient survival supports the notion that reduced mRNA methylation is positively linked to RAS-mediated oncogenic translation and subsequent cancer progression.

Reduced mRNA methylation promotes oncogenic translation

To validate the tumor suppressor role for METTL3 in cancers driven by oncogenic RAS signaling, we knocked down METTL3 from TtH cells bearing inducible RAS^{G12V}. With >80% depletion of METTL3, we observed approximately 40% reduction of mRNA m^{6}A levels (fig. S4D). This manipulation resembles the physiological status of mRNA methylation under oncogenic RAS expression. Translation of endogenous proteins was enhanced in cells with METTL3 knockdown as revealed by puromycin labeling (Fig. 4F). This result suggests that METTL3 depletion mimics the increased translation by oncogenic RAS. Consistently, real-time luciferase assay recorded elevated Fluc levels (1.8-fold) in the absence of METTL3. Upon 4-OHT treatment, despite the evident increase of overall Fluc levels, METTL3 knockdown did not further boost Fluc translation (Fig. 4G). Therefore, RAS-triggered oncogenic translation encompasses the effect of METTL3 reduction.

To test whether lowered m^{6}A levels on mRNAs directly leads to relaxation of initiation pausing, we conducted QTI-seq and Ribo-seq in TtH cells before and after METTL3 knockdown. A substantial number of transcripts (67.2%) showed reduced aTIS PI in cells lacking METTL3 (fig. S4E). Many of these transcripts had similar changes of aTIS PI in response to either METTL3 knockdown or RAS^{G12V} expression (fig. S4F), indicating that relaxed initiation pausing is a common feature shared by METTL3 depletion and oncogenic translation. In line with this notion, in cells lacking METTL3, the positive correlation of aTIS PI before and after 4-OHT treatment indicates that RAS^{G12V} expression had limited effects on initiation pausing (fig. S4G). We conclude that RAS-mediated oncogenic translation involves two distinct mechanisms: (i) activated eIF4F that enhances ribosome loading and (ii) relaxed initiation pausing that facilitates elongation commitment. The coordination between these two mechanisms maximizes translational flux during oncogenic translation (fig. S4H).

Increased mRNA methylation suppresses oncogenic translation

We next asked whether knocking down m^{6}A demethylases would counteract oncogenic translation by restoring initiation pausing via

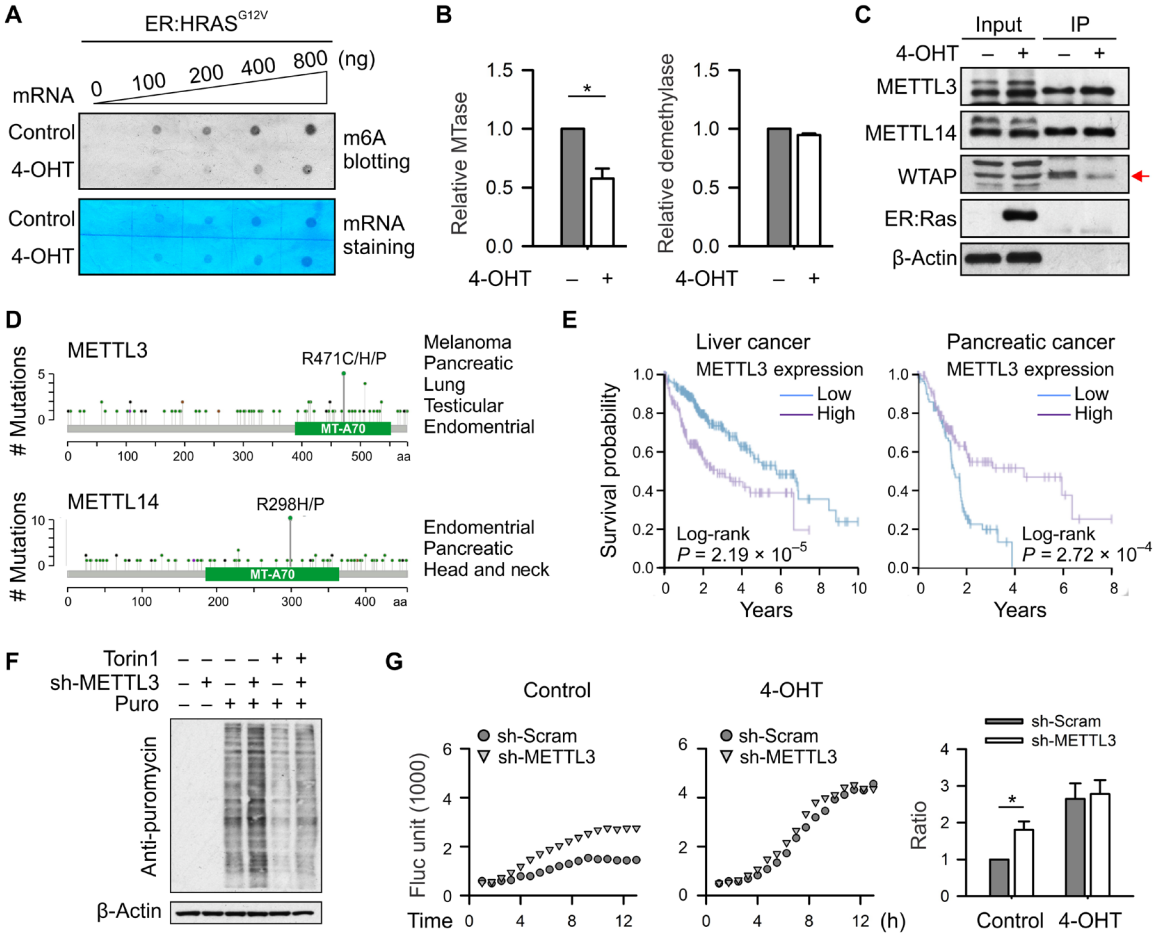

Fig. 4. Oncogenic RAS signaling reduces mRNA methylation. (**A**) m^{6}A dot blotting of mRNAs purified from TtH cells before and after RAS^{G12V} induction. Methylene blue staining was used for loading control. (**B**) m^{6}A methyltransferase (left) and demethylase (right) in cells before and after 4-OHT treatment. (**C**) Whole-cell lysates were immunoprecipitated using an anti-METTL3 antibody followed by Western blotting. (**D**) Derived from CBioPortal, the graphs show recurrent mutations in METTL3 and METTL14 observed in multiple cancer types listed on the right. MTase, methyltransferase; aa, amino acids. (**E**) Kaplan-Meier plot showing the association between expression of METTL3 and the overall survival of patients with liver cancer and pancreatic cancer. Log-rank *P* values are shown. (**F**) Puromycin-labeling assay in TtH cells with or without METTL3 knockdown, in the absence or presence of Torin1 treatment. (**G**) Real-time Fluc reporter assay in TtH cells with or without METTL3 knockdown, before or after RAS^{G12V} induction. The bar graphs show the relative Fluc levels at 10 hours post-transfection after normalization with mRNA levels. Error bars, means ± SEM; *$P < 0.05$, unpaired two tailed *t* test; $n = 3$ biological replicates (B and G).

increased mRNA methylation. In TtH cells without oncogenic RAS expression, knocking FTO had little effects on global protein synthesis measured by puromycin labeling (fig. S5A). This is likely due to the fact that transcripts with strong initiation pausing have limited room to increase methylation further. Cells lacking FTO showed no response to activated oncogenic RAS signaling after 4-OHT treatment as evidenced by comparable endogenous protein synthesis (Fig. 5A). Notably, these cells were still responsive to Torin1 treatment, indicating that the effect of FTO knockdown is independent of eIF4F. Consistently, real-time reporter assay revealed that the increased Fluc translation imposed by oncogenic RAS signaling was eliminated in the absence of FTO (Fig. 5B). To substantiate this finding further, we knocked down ALKBH5 and observed the similar translational consequence (fig. S5B). Therefore, elevated mRNA methylation effectively counteracts oncogenic translation induced by RAS signaling, presumably by canceling the relaxation of initiation pausing.

To assess whether increased mRNA methylation upon FTO knockdown is accompanied with restored initiation pausing, we took advantage of QTI-seq datasets obtained from HEK293 cells with either FTO knockdown or FTO overexpression (fig. S5, C and D). The aTIS ratio averaged across the entire transcriptome showed an approximate 1.5-fold increase in the absence of FTO, but nearly 40% decrease under FTO overexpression (Fig. 5C). When the methylated transcripts are considered, the fold change of aTIS PI at individual start codons is significantly increased in the absence of FTO compared to FTO overexpression (Wilcoxon signed-rank test, $P < 2.2 \times 10^{-16}$; Fig. 5D). For messages without m^{6}A modification near the start codon, changing FTO levels minimally affected initiation pausing (fig. S5D). The Ribo-seq variation could be due to the pleiotropic effect of FTO in mRNA stability and translation. Together with the effect of METTL3 knockdown (Fig. 4), these results indicate that mRNA methylation controls the translational output by modulating initiation pausing.

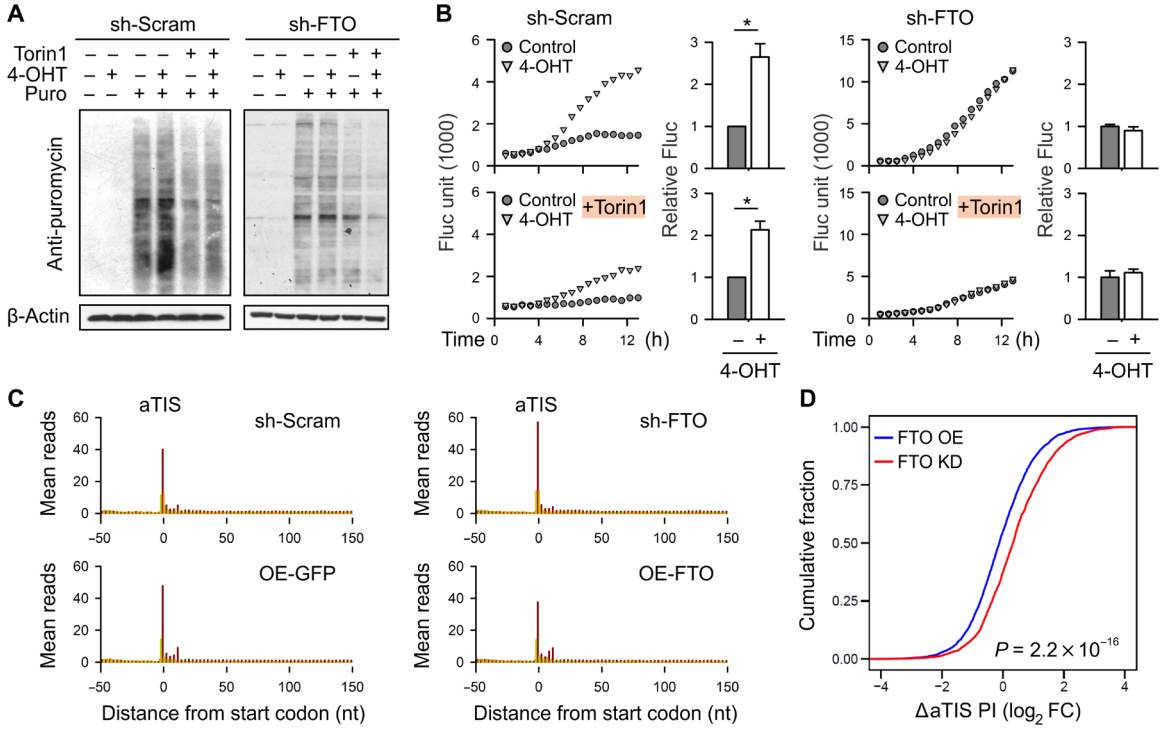

Fig. 5. FTO controls translational output by modulating initiation pausing. (**A**) Puromycin-labeling assay in TtH cells with or without FTO knockdown, before or after RAS^{G12V} induction, in the absence or presence of Torin1 treatment (50 nM for 2 hours). (**B**) Real-time Fluc reporter assay in TtH cells with or without FTO knockdown, before or after RAS^{G12V} induction, and in the absence or presence of Torin1 treatment (50 nM). The right panel shows the relative Fluc levels at 10 hours post-transfection after normalization with mRNA levels. Error bars, means ± SEM; *$P < 0.05$, unpaired two tailed *t* test; $n = 3$ biological replicates. (**C**) Metagene analysis of QTI-seq datasets derived from cells with either FTO knockdown or FTO overexpression (OE). GFP, green fluorescent protein. (**D**) Cumulative distribution plot depicting aTIS PI fold changes (FC) in cells with FTO knockdown (KD; red line) or FTO overexpression (blue line). Significance is calculated by Wilcoxon signed-rank test.

Restored initiation pausing prevents tumorigenesis

With only a subset of transcripts exhibiting initiation pausing, it is interesting to find the global translational effect in response to oncogenic RAS signaling. This is likely due to the fact that initiation pausing primarily restrains the translational flux for genes involving cell growth, especially the translation machinery (fig. S2, D to F). It is conceivable that increased translational capacity leads to increased global protein synthesis, which is essential for active proliferation of cancer cells. We next asked whether the lack of this translational "brake" alone contributes to cellular transformation and tumorigenesis. As expected, TtH cells with activated RAS^{G12V} expression readily formed colonies in soft agar (Fig. 6A). Since FTO knockdown restores initiation pausing, we explored the possibility of reversing oncogenic translation by depleting FTO from cells expressing RAS^{G12V}. Notably, FTO depletion mediated marked, sustained inhibition of colony formation (Fig. 6A).

To extend this finding from TtH cells to cancer cell lines derived from human patients, we examined two pancreatic cancer cell lines harboring $KRAS^{G12V}$ mutation (CFPAC-1) and $KRAS^{G12D}$ mutation (AsPC-1), respectively. Similar to TtH cells bearing inducible RAS^{G12V}, FTO knockdown significantly inhibited the colony formation in soft agar for both CFPAC-1 and AsPC-1 (Fig. 6B). To examine the tumorigenesis in vivo, we conducted xenograft experiments using immunocompromised severe combined immunodeficient (SCID)–Beige mice. Consistent with the colony formation assay, FTO knockdown significantly suppressed tumor growth following subcutaneous injection (Fig. 6C). We also selected a pancreatic cancer cell line BxPC-3 that harbors the wild-type KRAS. Unlike CFPAC-1 and AsPC-1, BxPC-3 failed to form colonies in soft agar. Intriguingly, FTO depletion exhibited little effects on the tumor growth of BxPC-3 in vivo (Fig. 6C, right). To substantiate this finding further, we conducted orthotopic implantation of pancreatic cancer cell lines with or without FTO knockdown into SCID mice. The orthotopic xenograft models have similar tumor microenvironment as the original tumor and more closely resemble the natural tumorigenesis in human. In agreement with the heterotopic tumor models, silencing FTO significantly inhibited the growth of tumor cells bearing RAS mutation but not the wild type (Fig. 6D). These results not only confirmed the cancer type specificity in terms of oncogenic translation but also excluded the possibility that the efficacy of FTO knockdown on mutant RAS cancers was a result of nonspecific effects.

Given the relaxed initiation pausing in the absence of METTL3, we wondered whether silencing METTL3 would promote tumorigenesis. In both orthotopic and heterotopic tumor models, depleting METTL3 further increased the tumor burden of CFPAC-1 and AsPC-1 despite their progressive nature (Fig. 6D and fig. S6). Once again, little difference was observed for the tumorigenesis of BxPC-3 cells. This result is in line with the tumor suppressor role for METTL3 in mutant RAS cancers.

Therapeutic potential of FTO inhibitors

Given the antitumor effect of FTO depletion, at least in RAS mutant cancers, we were encouraged to explore therapeutic potential of

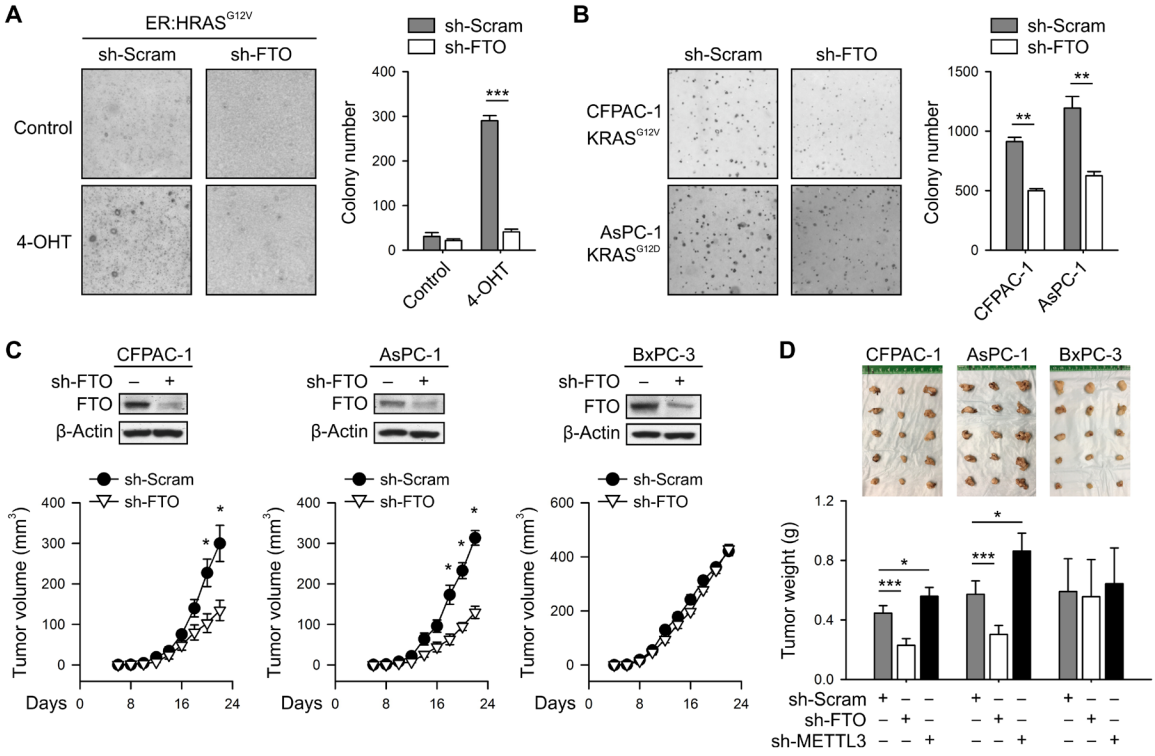

Fig. 6. Restored initiation pausing prevents tumorigenesis. (**A**) Representative images of soft agar colony formation assay for TtH cells with or without FTO knockdown, before (Control) or after RAS^{G12V} induction (4-OHT). The right panel shows quantification of colony formation assay. (**B**) Representative images of soft agar colony formation assay for the pancreatic cancer cell lines with or without FTO knockdown. The right panel shows quantification of colony formation assay. $^{**}P < 0.01$. (**C**) The pancreatic cancer cell lines CFPAC, AsPC-1, and BxPC-3 were subjected to FTO knockdown. Equal numbers of these cells were subcutaneously transplanted into SCID-Beige mice and the mean tumor volume is plotted over time. Error bars, means ± SEM; $^{*}P < 0.05$, unpaired two tailed *t* test; $n = 6$. (**D**) A total of 1×10^6 of CFPAC-1, AsPC-1, or BxPC-3 cells with either FTO or METTL3 knockdown were implanted into the pancreas of SCID mice. Tumors were harvested 5 weeks after inoculation followed by weight measurement. Photo credit, A. Zhou. Error bars, means ± SEM; $^{*}P < 0.05$, $^{***}P < 0.001$, unpaired two tailed *t* test; $n = 5$.

small-molecule inhibitors of FTO. Meclofenamic acid (MA), an anti-inflammatory drug, was previously shown to act as a selective inhibitor of FTO (*36*). However, the inhibition efficiency of MA is not satisfied. More recently, a more specific FTO inhibitor FB23-2 was developed and showed therapeutic potential for AML (*37*). Following the dose regime for AML, we assessed the therapeutic effects of FB23-2 in vivo with xenografted pancreatic cancers in SCID-Beige mice. A week after xenotransplantation, FB23-2 (10 mg/kg) or vehicle control was injected intraperitoneally into the individual mice every other day. FB23-2 administration significantly delayed the tumor growth of CFPAC-1 and AsPC-1 (Fig. 7, A and B). The little effect on the tumorigenesis of BxPC-3 not only confirms the therapeutic specificity of FB23-2 (Fig. 7C) but also indicates that the in vivo side effect of FTO inhibitors is minimal.

DISCUSSION

The translation machinery is centrally poised to support protein synthesis and biomass expansion to which malignant cells are addicted (*38*). Despite the wide belief that cap-dependent translation drives tumor progression, it is puzzling to find that inhibiting eIF4F alone does not completely eliminate oncogenic translation. Here, we report an additional checkpoint during translation initiation that involves start codon–associated ribosome pausing. Since ribosome initiation pausing selectively occurs on mRNAs involved in cell growth and proliferation, cancer cells apparently take advantage of relaxed ribosome pausing during oncogenic translation. By releasing the initiation brake, malignant cells achieve the maximum translational output as a result of increased ribosome loading to the 5′ end and rapid transition from initiation to elongation at the start codon. The coordination between eIF4F-mediated cap recognition and start codon–associated ribosome pausing fine-tunes the translational flux, which is co-opted by mutant RAS cancer cells to satisfy their increased anabolic demands.

Factors affecting the residence time of the 80*S* ribosome at the start codon are likely to be multifaceted. In addition to translation initiation factors such as eIF5B (*39*), distinct sequence features following individual start codons could contribute to the wide range of ribosome pausing across transcriptome. This possibility partially explains why QTI-seq does not capture the initiating ribosomes with the same efficiency (*25*, *40*). Nevertheless, differential initiation pausing on the same transcript must be due to factors beyond sequence. We unexpectedly found that m^{6}A modification in the start codon vicinity serves as a linchpin in this process. A common feature of mRNA methylation is the asymmetric distribution with most of the m^{6}A sites enriched near the stop codon (*41*, *42*). Notably, methylation levels at stop codons and 3′UTR are relatively static (*43*). By contrast, 5′UTR methylation is subject to dynamic regulation in response to different growth conditions (*44*). The start codon–associated m^{6}A enrichment was initially observed in plant species (*45*, *46*). A growing number of recent studies started to appreciate the relative enrichment of m^{6}A near start codons in various tissue

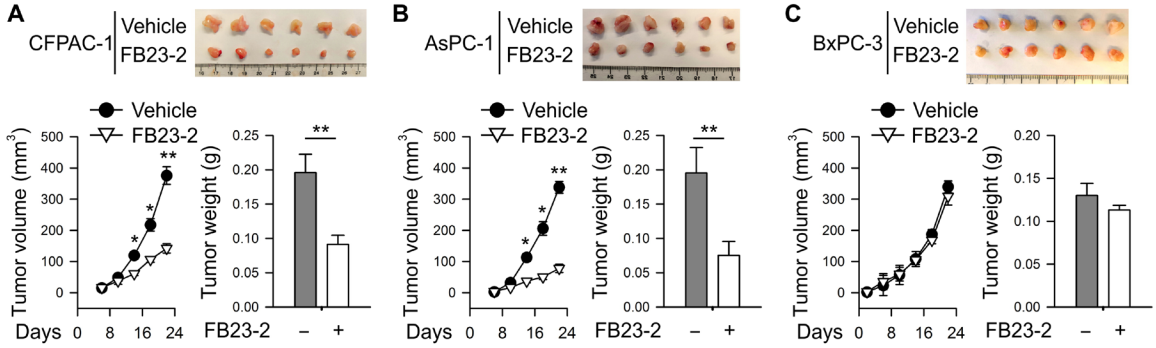

Fig. 7. Therapeutic potential of small-molecule FTO inhibitors. Equal number of CFPAC (**A**), AsPC-1 (**B**), and BxPC-3 (**C**) cells were subcutaneously transplanted into SCID-Beige mice. FB23-2 (10 mg/kg) or same volume of dimethyl sulfoxide was injected intraperitoneally into mice every other day. The mean tumor volume is plotted over time, and the tumor weight was measured at the end point. Photo credit, L. Dong. Error bars, means ± SEM; *$P < 0.05$, **$P < 0.01$, unpaired two tailed t test; $n = 6$.

samples, including cancers (*13*, *47*). However, the physiological significance of region-specific mRNA methylation remains poorly understood. For many transcripts, the strong correlation between the m^{6}A modification near the start codons and initiation pausing represents an additional layer of translational regulation. How exactly mRNA methylation in the start codon vicinity leads to initiation pausing warrants further investigation. We have searched for potential "readers" in m^{6}A-controlled initiation pausing by examining published crosslinking immunoprecipitation (CLIP)-based datasets. However, all YTH family proteins (DF1, DF2, DF3, DC1, and DC2) do not seem to have their binding sites enriched around start codons (*48*). One plausible mechanism could involve eIF3 that plays critical roles in ribosome scanning and start codon selection. In particular, 80*S* ribosome–associated eIF3 has been reported to be crucial in translation reinitiation (*49*). Since eIF3 has been proposed to interact with m^{6}A (*50*), we hypothesized that eIF3 could possibly retain the 80*S* ribosome at the start codon via interaction with m^{6}A and subsequently delay the elongation commitment.

Perhaps the most unexpected finding is the decreased mRNA methylation by oncogenic RAS signaling. The mechanistic connection between m^{6}A and cancer-relevant processes was initially suggested from studies linking m^{6}A to cellular differentiation pathways that control the stem cell fate. A series of recent studies reported that mRNA m^{6}A modification plays a critical role in the development of cancers such as AML and glioblastoma (*12*–*14*). While depleting m^{6}A methyltransferases promoted tumorigenesis, knocking down FTO or ALKBH5 suppresses tumor progression. These results clearly point to a link between altered m^{6}A levels and tumorigenesis, although few mechanistic details are currently known. It is noteworthy that the mRNA methylation program has a context-dependent effect on tumorigenesis. The consequences of m^{6}A modifications can be complex and dependent on cellular identity as well as differentiation status (*51*). Depending on cell types, loss of m^{6}A has been shown to yield different outcomes. In addition, tumor initiation and maintenance could involve different cellular programs. It will be interesting to demonstrate the role of m^{6}A in early and late stages of tumor progression. The reduced METTL3 expression during RAS oncogenic translation is in line with the poor survival in patients with pancreatic cancer (Fig. 4D). In addition, the missense mutations of m^{6}A methyltransferases found in pancreatic and endometrial cancers are associated with reduced methyltransferase activities (*15*). Collectively, oncogenic RAS signaling drives cancer development and progression by coordinating increased ribosome loading and relaxed initiation pausing.

The complex phenotype of m^{6}A in cancer biology could also be attributed to the pleiotropic effects of mRNA methylation in cellular processes ranging from mRNA splicing, polyadenylation, mRNA export, translation, to degradation. However, in cells with oncogenic RAS signaling, we found limited changes of mRNA steady-state levels despite reduced mRNA methylation (Fig. 2). It is also worth noting that altering global m^{6}A levels has limited effects on tumorigenesis of pancreatic cancer cells with wild-type RAS (Fig. 6D), arguing against the global effects of altered m^{6}A levels. It further substantiates the notion that the translational effects of initiation pausing are coupled with oncogenic signaling. The discovery that m^{6}A modification in the vicinity of start codons influences the behavior of initiating ribosomes greatly expands the breadth of physiological roles of "epitranscriptomics" in translational regulation.

Mutant RAS-driven cancers are extremely refractory to standard chemotherapeutic treatments (*52*, *53*). There is a dire need for new therapeutic approaches that are likely based on a better understanding of the biology of this disease. The functional connection between reduced mRNA methylation and relaxed initiation pausing during oncogenic translation creates vulnerabilities for mutant RAS cancer cells that could be exploited as a therapeutic strategy. In this regard, FTO knockdown or FTO inhibitors offer a promising strategy for reversing oncogenic translation (*36*, *54*). Our study demonstrates the feasibility of attenuated FTO demethylation for the inhibition of oncogenic translation. With the functional diversity of mRNA methylation on the rise, it will be highly desirable to control m^{6}A modification in a transcript- and site-specific manner. We envision that compounds capable of adjusting ribosome initiation pausing may increase the efficacy of current cancer therapy regime.

MATERIALS AND METHODS

Cell lines and reagents

Primary TtH cells were stably infected to generate polyclonal populations with retrovirus derived from pBabe Puro by subcloning into complementary DNA (cDNA) encoding fused ER:HRas^{G12V}. The primary TtH cells and ER:HRas^{G12V} TtH cells were maintained in Dulbecco's modified Eagle's medium (DMEM) with 10% fetal bovine serum (FBS). ER:HRas^{G12V} TtH cells were treated with 1 μM 4-OHT (Sigma-Aldrich) for 48 hours for oncogenic HRas^{G12V} expression; BxPC-3 (KRas^{WT}), and AsPC-1 (KRas^{G12D}) cells were grown in RPMI 1640 medium with 10% FBS; CFPAC-1 (KRas^{G12V}) cells were grown in Iscove's modified Dulbecco's medium with 10% FBS.

Antibodies used in this study are listed as follows: anti–pan-Ras [Milipore MABS195, 1:1000 Western blotting (WB)], anti-Akt (Cell Signaling Technology, 9272; 1:1000 WB), anti–phospho (Ser^{473})–Akt (Cell Signaling Technology, 9271; 1:1000 WB), anti-p70 S6 kinase (Cell Signaling Technology, 9202; 1:1000 WB), anti–phospho-S6 (Thr^{389}) kinase (Cell Signaling Technology, 9205; 1:1000 WB), anti–4E-BP1 (Cell Signaling Technology, 9452; 1:1000 WB), anti–phospho ($Thr^{37/46}$) 4E-BP1 (Cell Signaling Technology, 2855; 1:1000 WB), anti-METTL3 (Abnova, H00056339-B01P; 1:1000 WB), anti-METTL14 (Sigma-Aldrich, HPA038002; 1:1000 WB), anti-WTAP (Santa Cruz Biotechnology, sc-374280; 1:1000 WB), anti-FTO (PhosphoSolutions, 597-FTO; 1:1000 WB), anti-ALKBH5 (Proteintech, 16837-1-AP; 1:1000 WB), anti-YTHDF1 (Proteintech, 17479-1-AP; 1:1000 WB), anti-YTHDF2 (Proteintech, 24744-1-AP; 1:1000 WB), anti-m^6A (Millipore, ABE572; 1:1000 WB), anti-puromycin (Developmental Studies Hybridoma Bank, PMY-2A4; 1:100 WB) and anti–β-actin (Sigma-Aldrich, A5441; 1:2000 WB).

Lentiviral short hairpin RNAs

Short hairpin RNA (shRNA) targeting sequences based on The RNAi Consortium at Broad Institute (https://portals.broadinstitute.org/gpp/public/) are listed below: METTL3 (human): 5′-ATTCTGTGACTATGGAACCA-3′; FTO (human): 5′-GCCAGTGAAAGGGTCTAATAT-3′; and scramble control sequence: 5′-AACAGTCGCGTTTGCGACTGG-3′. shRNA targeting sequences were cloned into DECIPHER pRSI9-U6-(sh)-UbiC-TagRFP-2A-Puro (Cellecta, CA). Lentiviral particles were packaged using Lenti-X 293 T cells (Clontech). Virus-containing supernatants were collected at 48 hours after transfection and filtered to eliminate cells. Cells were infected by the lentivirus for 48 hours before selection by puromycin (1 to 2 μg ml^{-1}).

Immunoblotting

Immunoblotting was conducted using a method described previously (*44*). In brief, cells were lysed on ice in tris-buffered saline (TBS) buffer [50 mM tris (pH 7.5), 150 mM NaCl, and 1 mM EDTA] containing a protease inhibitor cocktail tablet, 1% Triton X-100, and deoxyribonuclease (2 U ml^{-1}). After incubating on ice for 30 min, the lysates were heated for 5 min, 95°C in SDS–polyacrylamide gel electrophoresis (SDS-PAGE) sample buffer [50 mM tris (pH 6.8), 100 mM dithiothreitol (DTT), 2% SDS, 0.1% bromophenol blue, and 10% glycerol]. Proteins were separated on an SDS–polyacrylamide gel and transferred to Immobilon-P membranes (Millipore). Membranes were blocked for 1 hour in TBS containing 5% nonfat milk and 0.1% Tween 20, followed by incubation with primary antibodies overnight at 4°C. After incubation with horseradish peroxidase (HRP)–coupled secondary antibodies at room temperature for 1 hour, immunoblots were visualized using enhanced chemiluminescence (ECL^{Plus}, GE Healthcare).

Soft agar colony formation assay

Bottom agar layer was made with 0.8% noble agar (Sigma-Aldrich, A5431) in growth medium with 10% FBS in a six-well plate (1.5 ml per well). Cells were detached with trypsin-EDTA, washed twice with Dulbecco's Phosphate Buffered Saline (DPBS) and counted, and 0.4% noble agar in growth medium mixed with single suspended cells (10^4 per well) was placed on top of a solidified bottom agar. Cells were fed twice a week with 500-μl growth medium with 10% FBS. After 3 to 4 weeks of growing, the colonies were counted and imaged using a dissecting microscope.

Xenograft injections

Cells at 70 to 80% confluence were changed with fresh medium to remove the dead cells 3 to 4 hours before harvesting, then detached with trypsin-EDTA, and washed twice with DPBS. Cells were counted after collection, and 5×10^6 cells were suspended in 50-μl DPBS in combination with 50-μl Matrigel (BD Biosciences, 356234). A total of 100 μl was injected subcutaneously into each side of the lower flank of the SCID-Beige mice (6 to 8 weeks of age) using insulin syringes. For testing the therapeutic potential of FTO inhibitor, 100-μl FB23-2 [dissolved in dimethyl sulfoxide (DMSO), 10 mg/kg mouse weight] or same volume of DMSO was injected intraperitoneally into mice every other day. Mice were examined every other day for evidence of tumor growth. Tumor diameters were measured with calipers, and the tumor volume in cubic millimeter was calculated by the formula: Volume = $(\text{width})^2 \times \text{length}/2$. Tumor tissues were excised after tumors reached a diameter of 10 mm (3 to 4 weeks). Mice were housed in a temperature- and humidity-controlled facility with a 12-hour light-dark cycle. The experimental protocols were approved by Cornell Institutional Animal Care and Use Committee (no. 2008-0167).

Orthotopic mouse model of pancreatic tumor growth

All animals were maintained in facilities approved by the Association for Assessment and Accreditation of Laboratory Animal Care International in accordance with the current regulations and standards of the U.S. Department of Agriculture and Department of Health and Human Services. The sample sizes of the animals were justified by statistical considerations and statistical power analyses. The animals were randomized to different experimental groups. For tumorigenic assay using an orthotopic mouse model, AsPC-1, CFPAC-1, or BxPC-3 cells (1×10^6 cells per mouse, 5 mice per group) in 0.1 ml of Hanks' balanced salt solution were injected into the pancreases of 7- to 8-week-old female athymic BALB/c nude mice (National Cancer Institute, Fredrick, MD), respectively. The mice were euthanized 4 to 5 weeks after tumor cell inoculation, and their tumors were harvested and weighed. The investigators were blinded to allocation during experiments and outcome assessment.

In vitro m^6A methyltransferase activity assay

$ER:HRas^{G12V}$ cells with or without 48-hour 4-OHT treatment (1 μM) were lysed in denaturing lysis buffer [20 mM tris-HCl (pH 7.5), 137 mM NaCl, 1% NP-40, and 2 mM EDTA] after three times wash with cold DPBS, then incubated at 4°C for 30 min with rotation, followed by centrifuging at 12,000 rpm for 15 min. The supernatant were collected and the concentration of total protein was measured using 660-nm protein assay reagent (Pierce). The in vitro methylation assay was performed in a 50-μl reaction mixture containing 400 nM RNA probe (commercially synthesized in vitro, Thermo Fisher Scientific), cell lysate with same amount of total protein, 20 mM tris (pH 7.5), 50 μM $ZnCl_2$, 1 mM DTT, RNaseOUT (0.2 U/μl), 1% glycerol, and 0.5 μCi [methyl-3H]AdoMet (PerkinElmer). The reaction was incubated at 30°C for 1 hour and then stopped by adding TRIzol reagent (Invitrogen). RNA after reaction was precipitated and purified using sodium acetate at −20°C for at least 2 hours. The precipitated RNA was subjected to radioactivity measurement using scintillation counting (Beckman). Levels of ^3H-methyl–incorporated RNA are shown as disintegrations per minute.

Real-time quantitative polymerase chain reaction

Real-time quantitative polymerase chain reaction (qPCR) was conducted using a method described previously (*44*). In brief, total RNA was isolated with TRIzol reagent (Invitrogen), and reverse transcription was performed using the High Capacity cDNA Reverse Transcription Kit (Invitrogen). Real-time PCR analysis was conducted using Power SYBR Green PCR Master Mix (Applied Biosystems) and carried on a LightCycler 480 Real-Time PCR System (Roche Applied Science). All primers used in this study are listed in table S1.

Real-time luciferase assay

Real-time luciferase assay was conducted using a method described previously (*44*). In brief, cells grown in 35-mm dishes were transfected with 1-μg plasmids including luciferase gene (PGL3-luciferase or pcDNA3-CMV-luciferase) at 70 to 80% confluence. Luciferase substrate D-luciferin (1 mM, Regis Technologies) was added into the culture medium immediately after transfection. Luciferase activity was monitored continuously and recorded using Kronos Dio Luminometer (Atto).

Puromycin labeling

As described previously (*55*), cells at 70 to 80% confluence were treated with puromycin (10 μg ml^{-1}) for 10 min. After washing twice with ice-cold DPBS, cells were lysed with SDS-PAGE sample buffer, and proteins were separated on SDS-PAGE and transferred to Immobilon-P membranes. Membranes were blocked for 1 hour in TBS containing 5% nonfat milk and 0.1% Tween 20, followed by incubation with puromycin antibodies (1:100 dilution) overnight at 4°C. After incubation with HRP-conjugated anti-mouse immunoglobulin G (IgG) (1:5000 dilution) for 1 hour at room temperature, the membrane was visualized using enhanced chemiluminescence.

[^{35}S] methionine radiolabeling

ER:$HRas^{G12V}$ cells with or without 4-OHT treatment (1 μM for 48 hours) and Torin1 treatment (10 nM or 100 nM for 2 hours) were washed with DPBS before incubation in methionine-free DMEM for 15 min. Cells were resuspended in labeling media {methionine-free DMEM supplemented with 10% FBS and methionine (30 μCi ml^{-1} [^{35}S])} for 15 min. Labeling was stopped by ice-cold DMEM containing cycloheximide (100 μg ml^{-1}). Cells were washed with DPBS containing cycloheximide (100 μg ml^{-1}), lysed with SDS sample loading buffer. Cell lysates were heated and then resolved on a 10% tris-glycine SDS-PAGE gel, and radiography captured was by Typhoon 9400.

m^{6}A dot blotting

Total cellular RNAs were isolated with TRIzol reagent, and mRNAs were purified using Dynabeads Oligo $(dT)_{25}$ (Thermo Fisher Scientific). Equal amounts of mRNA were spotted to a Hybond-N^+ membrane (GE Healthcare), followed by ultraviolet (UV) cross-linking at UV 254 nm (0.12 J/cm^2). After blocking in DPBS containing 5% nonfat milk and 0.1% Tween 20 for 1 hour, the membrane was incubated with anti-m^{6}A antibody (1:1000 dilution) overnight at 4°C. The membrane was incubated with HRP-conjugated anti-rabbit IgG (1:5000 dilution) at room temperature for 1 hour and visualized using enhanced chemiluminescence.

Preparation of cell lysates for Ribo-seq and QTI-seq

As described previously (*25*), at least four 10-cm dishes of cells were harvested in 400-μl ice-cold polysome buffer [10 mM Hepes (pH 7.4), 100 mM KCl, and 5 mM $MgCl_2$] containing cycloheximide (100 μg ml^{-1}, for Ribo-seq) or lactimidomycin (5 μM, for QTI-seq). As described previously (*25*), cells were then disrupted by vortexing six times for 20 s using lysing matrix D (Fisher), followed by a 40-s interval each time on ice and then centrifuged at 12,000*g*, 4°C for 10 min. For QTI-seq, to dissociate noninitiating ribosomes, cell lysates were incubated in a solution containing 16 mM Hepes buffer (pH 7.4), 10 mM creatine phosphate, 0.1 mM spermidine, creatine phosphokinase (40 μg ml^{-1}), 0.8 mM adenosine triphosphate (ATP), and 25 μM puromycin at 35°C for 15 min. Samples were then subjected to sucrose gradient sedimentation.

Polysome profiling

As described previously (*25*), sucrose solutions were prepared in polysome buffer [10 mM Hepes (pH 7.4), 100 mM KCl, 5 mM $MgCl_2$, and 2% Triton X-100]. Fifteen to 45% (w/v) sucrose density gradients were freshly prepared in SW41 ultracentrifuge tubes (Backman) using a Gradient Master (BioComp Instruments). Five hundred microliters of supernatant from cell lysates prepared as described above was loaded onto sucrose gradients followed by centrifugation for 2.5 hours at 32,000 rpm, 4°C in a SW41 rotor. Separated samples were fractionated at 1.5 ml min^{-1} through an automated fractionation system (Isco) that continually monitors values of optical density at 254 nm.

RNA-seq and m^{6}A-seq

Both RNA-seq and m^{6}A-seq procedures have been described previously (*44*). For RNA-seq, total RNA was first isolated using TRIzol reagent followed by fragmentation using freshly prepared RNA fragmentation buffer [10 mM tris-HCl (pH 7.0) and 10 mM $ZnCl_2$]. Five-microgram fragmented RNA was saved as input control. For m^{6}A IP, 1-mg fragmented RNA was incubated with 15-μg anti-m^{6}A antibody (Millipore ABE572) in 1× IP buffer [10 mM tris-HCl (pH 7.4), 150 mM NaCl, and 0.1% Igepal CA-630] for 2 hours at 4°C. The m^{6}A-IP mixture was then incubated with protein A beads for additional 2 hours at 4°C on a rotating wheel. After washing three times with IP buffer, bound RNA was eluted using 100-μl elution buffer (6.7 mM N^6-methyladenosine 5′-monophosphate sodium salt in 1× IP buffer), followed by ethanol precipitation. Precipitated RNA was used for cDNA library construction and high-throughput sequencing described below.

SELECT

All primers used in SELECT are listed in table S2. Five-microliter total RNA was mixed with 40 nM Up Primer, 40 nM Down Primer, and 5 μM deoxynucleotide triphosphate (dNTP) in 17-μl 1× CutSmart buffer [50 mM KAc, 20 mM tris-HAc, 10 mM $MgAc_2$, and bovine serum albumin (100 μg/ml; pH 7.9) at 25°C]. The RNA and primers were annealed by incubating at 90°C for 1 min, 80°C for 1 min, 70°C for 1 min, 60°C for 1 min, 50°C for 1 min, and then 40°C for 6 min. Subsequently, 3 μl of mixture containing 0.01 U of *Bst* 2.0 DNA polymerase, 0.5 U of SplintR ligase, and 10 nmol of ATP was added to the final volume of 20 μl. The final reaction mixture was incubated at 40°C for 20 min and then denatured at 80°C for 20 min. Ten-microliter qPCR reaction was set up with 2× Power SYBR Green PCR Master Mix (Applied Biosystems), 200 nM qPCR-F primer, 200 nM qPCR-R primer, and 2.5 μl of the final reaction mixture. qPCR was run at the following conditions: 95°C, 1 min; (95°C, 10 s; 60°C, 45 s) × 45 cycles.

cDNA library construction

As described previously (*25*), *Escherichia coli* ribonuclease I (Ambion, 750 U per 100 units of absorbance at 260 nm) was added into the pooled fractions from ribosome profiling and incubated at 4°C for 1 hour, and then total RNAs were extracted using TRIzol reagent. RNA extracts (Ribo-seq and QTI-seq), fragmented RNAs (RNA-seq), and m^{6}A-IP elutes (m6A-seq) were dephosphorylated for 2 hours at 37°C in a 15-μl reaction (1× T4 polynucleotide kinase buffer, 10 U of SUPERase_In, and 20 U of T4 polynucleotide kinase). The products were separated on a 15% polyacrylamide tris-borate EDTA (TBE)–urea gel (Invitrogen) and visualized using SYBR Gold (Invitrogen). Selected regions in the gel corresponding to 40 to 60 nt (for RNA-seq and m^{6}A-seq) or 25 to 35 nt (for Ribo-seq and QTI-seq) were excised. The gel slices were disrupted by using centrifugation through the holes at the bottom of the tube. RNA fragments were dissolved by soaking overnight in 400-μl RNA elution buffer [300 mM NaOAc (pH 5.2), 1 mM EDTA, and SUPERase_In (0.1 U ml^{-1})]. The gel debris was removed using a Spin-X column (Corning), followed by ethanol precipitation. Purified RNA fragments were resuspended in nuclease-free water. Poly(A) tailing reaction was carried out for 45 min at 37°C [1× poly(A) polymerase buffer, 1 mM ATP, SUPERase_In (0.75 U μl^{-1}), and 3 U of *E. coli* poly(A) polymerase].

For reverse transcription, the oligos containing barcodes were listed in table S3. In brief, the tailed-RNA sample was mixed with 0.5 mM dNTP and 2.5 mM synthesized primer and incubated at 65°C for 5 min, followed by incubation on ice for 5 min. The reaction mix was then added with 20 mM tris (pH 8.4), 50 mM KCl, 5 mM $MgCl_2$, 10 mM DTT, 40 U of RNaseOUT, and 200 U of SuperScript III. Reverse transcription reaction was performed according to the manufacturer's instruction. Reverse transcription products were separated on a 10% polyacrylamide TBE-urea gel as described earlier. The extended first-strand product band was expected to be approximately 100 nt, and the corresponding region was excised. The cDNA was recovered by using DNA gel elution buffer (300 mM NaCl and 1 mM EDTA). First-strand cDNA was circularized in 20 μl of reaction containing 1× CircLigase buffer, 2.5 mM $MnCl_2$, 1 M betaine, and 100 U of CircLigase II (Epicentre). Circularization was performed at 60°C for 1 hour, and the reaction was heat-inactivated at 80°C for 10 min and then was precipitated by ethanol.

Deep sequencing

As described previously (*25*), circular template was amplified by PCR by using the Phusion high-fidelity (HF) enzyme (New England Biolabs) according to the manufacturer's instructions. The oligonucleotide primers listed in table S3 were used to create DNA suitable for sequencing. The PCR contains 1× HF buffer, 0.2 mM dNTP, 0.5 μM oligonucleotide primers, and 0.5 U of Phusion polymerase. PCR was carried out with an initial 30-s denaturation at 98°C, followed by 12 cycles of 10-s denaturation at 98°C, 20-s annealing at 60°C, and 10-s extension at 72°C. PCR products were separated on a nondenaturing 8% polyacrylamide TBE gel as described earlier. Expected DNA at 120 base pairs was excised and recovered as described earlier. After quantification by Agilent BioAnalyzer DNA 1000 assay, equal amounts of barcoded samples were pooled into one sample. Approximately 5 pM mixed DNA samples were used for cluster generation followed by sequencing by using sequencing primer 5′-CGACAGGTTCAGAGTTCTACAGTCCGACGATC-3′ (Illumina HiSeq).

Alignment of sequencing reads

The 3′ adapters and low-quality bases were trimmed by Cutadapt as described previously (*48*). The trimmed reads with length <15 nt were excluded. For Ribo-seq and QTI-seq, reads without adapters were discarded. The remaining reads were mapped to the human transcriptome using Bowtie with parameters: -a --best -m1 --strata. The annotation file downloaded from ENSEMBL database (GRCh38) was used to construct the transcriptome index file. For each gene, the transcript with longest CDS was selected. In the case of equal CDS length, the longest transcript was used. For read alignment, two mismatches were permitted. To avoid ambiguity, the reads mapped to multiple positions were disregarded for further analyses. The 13th, 14th, and 15th positions (12-nt offset from the 5′ end) of the resulting uniquely mapped read was defined as the ribosome P-site position. For Ribo-seq, the reads mapped to CDS were used to calculate the RPKM (reads per kilobase of transcript per million mapped reads) values for translation levels. For RNA-seq, the reads mapped to entire transcript were used to calculate RPKM. Transcripts with RPKM <1 were excluded. Translation efficiency was defined as the ratio of RPKM of Ribo-seq over RPKM of RNA-seq.

Calculation of PI at the start codon

For each transcript, QTI-seq reads with the P-site in a window centering the annotated start codon (−5, +5 nt) were used to represent the abundance of translation initiation signal at the start codon, which we termed aTIS density. PI was defined as the ratio of mean aTIS density in the window over mean read captured by QTI-seq in the remaining CDS region. To reduce the noises from insufficiently translating mRNAs, which usually result in a large variation on PI estimation, we only considered the mRNAs that meet the following criteria: (i) RPKM estimated by Ribo-seq was higher than 1. (ii) aTIS density in the window either in wild-type or 4-OHT treatment sample was higher than 3. For the transcripts with 0 value of aTIS density, a pseudo-number 1 was used. The mean value by averaging PIs of two replicates was used in analyses. The transcripts with top (bottom) 20% of aTIS PI were defined as high (low) aTIS PI transcripts.

m^{6}A sites identification and aggregation plot

m^{6}A sites were identified using the method described previously (*48*). m^{6}A coverages at individual sites were normalized by the mean coverage of the transcript. To avoid possible biases caused by insufficient coverage, analyses were limited to the transcripts with at least 30 reads per 1000 nt. Then, all transcripts were divided into three segments: 5′UTR, CDS, and 3′UTR. Each segment was then divided into 100 bins with equal length. All transcripts were aggregated by averaging the normalized m^{6}A coverages across all available transcripts embracing the same bins. Besides aggregation plot in normalized mRNA regions, we also aggregated m^{6}A coverages around the start codon (−300, +400), without normalizing the length of mRNA regions.

RNA secondary structure analysis

A sliding window of 30 nt with a step of 3 nt was used to calculate RNA minimum fold free energy (MFE) along transcript. For each window, MFE was calculated by ViennaRNA (*56*), using default parameters. For aggregation plot, a mean MFE in each window was calculated by averaging MFE values of the windows at the same position. DMS-seq data were used to investigate mRNA folding in vivo. DMS signal and Gini score were calculated using the methods in the

work of Rouskin *et al.* (*57*). PARS data were used to analyze mRNA secondary structure in vitro (*58*).

Gene GO analysis

DAVID was used for GO enrichment analysis. The genes with fold change higher than 2 or lower than 0.5 were used for GO analysis. The expressed genes (FPKM >1) were used as the background gene set. Pathway analysis was performed by ClueGO (*59*) based on the annotation of Reactome (*60*).

Code availability

All statistical analyses were performed by R. The heatmap plots were made by heatmap.2 in R. All procedures but sequencing mapping were completed using custom Perl scripts. These scripts are available upon request.

SUPPLEMENTARY MATERIALS

Supplementary material for this article is available at http://advances.sciencemag.org/cgi/content/full/7/8/eabd6927/DC1

View/request a protocol for this paper from *Bio-protocol*.

REFERENCES AND NOTES

1. D. Silvera, S. C. Formenti, R. J. Schneider, Translational control in cancer. *Nat. Rev. Cancer* **10**, 254–266 (2010).
2. M. Bhat, N. Robichaud, L. Hulea, N. Sonenberg, J. Pelletier, I. Topisirovic, Targeting the translation machinery in cancer. *Nat. Rev. Drug Discov.* **14**, 261–278 (2015).
3. M. L. Truitt, D. Ruggero, New frontiers in translational control of the cancer genome. *Nat. Rev. Cancer* **16**, 288–304 (2016).
4. R. J. Shaw, L. C. Cantley, Ras, PI(3)K and mTOR signalling controls tumour cell growth. *Nature* **441**, 424–430 (2006).
5. M. D. Cole, V. H. Cowling, Transcription-independent functions of MYC: Regulation of translation and DNA replication. *Nat. Rev. Mol. Cell Biol.* **9**, 810–815 (2008).
6. X. M. Ma, J. Blenis, Molecular mechanisms of mTOR-mediated translational control. *Nat. Rev. Mol. Cell Biol.* **10**, 307–318 (2009).
7. J. Pelletier, J. Graff, D. Ruggero, N. Sonenberg, Targeting the eIF4F translation initiation complex: A critical nexus for cancer development. *Cancer Res.* **75**, 250–263 (2015).
8. B. Markman, R. Dienstmann, J. Tabernero, Targeting the PI3K/Akt/mTOR pathway–beyond rapalogs. *Oncotarget* **1**, 530–543 (2010).
9. A. G. Hinnebusch, The scanning mechanism of eukaryotic translation initiation. *Annu. Rev. Biochem.* **83**, 779–812 (2014).
10. I. A. Roundtree, M. E. Evans, T. Pan, C. He, Dynamic RNA nodifications in gene expression regulation. *Cell* **169**, 1187–1200 (2017).
11. C. Zhang, D. Samanta, H. Lu, J. W. Bullen, H. Zhang, I. Chen, X. He, G. L. Semenza, Hypoxia induces the breast cancer stem cell phenotype by HIF-dependent and ALKBH5-mediated m^{6}A-demethylation of NANOG mRNA. *Proc. Natl. Acad. Sci. U.S.A.* **113**, E2047–E2056 (2016).
12. Z. Li, H. Weng, R. Su, X. Weng, Z. Zuo, C. Li, H. Huang, S. Nachtergaele, L. Dong, C. Hu, X. Qin, L. Tang, Y. Wang, G.-M. Hong, H. Huang, X. Wang, P. Chen, S. Gurbuxani, S. Arnovitz, Y. Li, S. Li, J. Strong, M. B. Neilly, R. A. Larson, X. Jiang, P. Zhang, J. Jin, C. He, J. Chen, FTO plays an oncogenic role in acute myeloid leukemia as a N^6-Methyladenosine RNA demethylase. *Cancer Cell* **31**, 127–141 (2017).
13. Q. Cui, H. Shi, P. Ye, L. Li, Q. Qu, G. Sun, G. Sun, Z. Lu, Y. Huang, C.-G. Yang, A. D. Riggs, C. He, Y. Shi, m^{6}A RNA methylation regulates the self-renewal and tumorigenesis of glioblastoma stem cells. *Cell Rep.* **18**, 2622–2634 (2017).
14. S. Zhang, B. S. Zhao, A. Zhou, K. Lin, S. Zheng, Z. Lu, Y. Chen, E. P. Sulman, K. Xie, O. Bögler, S. Majumder, C. He, S. Huang, m^{6}A demethylase ALKBH5 maintains tumorigenicity of glioblastoma stem-like cells by sustaining FOXM1 expression and cell proliferation program. *Cancer Cell* **31**, 591–606.e6 (2017).
15. J. Liu, M. A. Eckert, B. T. Harada, S.-M. Liu, Z. Lu, K. Yu, S. M. Tienda, A. Chryplewicz, A. C. Zhu, Y. Yang, J.-T. Huang, S.-M. Chen, Z.-G. Xu, X.-H. Leng, X.-C. Yu, J. Cao, Z. Zhang, J. Liu, E. Lengyel, C. He, m^{6}A mRNA methylation regulates AKT activity to promote the proliferation and tumorigenicity of endometrial cancer. *Nat. Cell Biol.* **20**, 1074–1083 (2018).
16. S. Lin, J. Choe, P. Du, R. Triboulet, R. I. Gregory, The m(6)A methyltransferase METTL3 promotes translation in human cancer cells. *Mol. Cell* **62**, 335–345 (2016).
17. L. P. Vu, B. F. Pickering, Y. Cheng, S. Zaccara, D. Nguyen, G. Minuesa, T. Chou, A. Chow, Y. Saletore, M. M. Kay, J. Schulman, C. Famulare, M. Patel, V. M. Klimek, F. E. Garrett-Bakelman, A. Melnick, M. Carroll, C. E. Mason, S. R. Jaffrey, M. G. Kharas, The N^6-methyladenosine (m^{6}A)-forming enzyme METTL3 controls myeloid differentiation of normal hematopoietic and leukemia cells. *Nat. Med.* **23**, 1369–1376 (2017).
18. Y. Pylayeva-Gupta, E. Grabocka, D. Bar-Sagi, RAS oncogenes: Weaving a tumorigenic web. *Nat. Rev. Cancer* **11**, 761–774 (2011).
19. B. Papke, C. J. Der, Drugging RAS: Know the enemy. *Science* **355**, 1158–1163 (2017).
20. M. A. Collins, F. Bednar, Y. Zhang, J.-C. Brisset, S. Galbán, C. J. Galbán, S. Rakshit, K. S. Flannagan, N. V. Adsay, M. P. di Magliano, Oncogenic Kras is required for both the initiation and maintenance of pancreatic cancer in mice. *J. Clin. Invest.* **122**, 639–653 (2012).
21. K.-H. Lim, C. M. Counter, Reduction in the requirement of oncogenic Ras signaling to activation of PI3K/AKT pathway during tumor maintenance. *Cancer Cell* **8**, 381–392 (2005).
22. C. C. Thoreen, S. A. Kang, J. W. Chang, Q. Liu, J. Zhang, Y. Gao, L. J. Reichling, T. Sim, D. M. Sabatini, N. S. Gray, An ATP-competitive mammalian target of rapamycin inhibitor reveals rapamycin-resistant functions of mTORC1. *J. Biol. Chem.* **284**, 8023–8032 (2009).
23. N. T. Ingolia, S. Ghaemmaghami, J. R. S. Newman, J. S. Weissman, Genome-wide analysis in vivo of translation with nucleotide resolution using ribosome profiling. *Science* **324**, 218–223 (2009).
24. G. A. Brar, J. S. Weissman, Ribosome profiling reveals the what, when, where and how of protein synthesis. *Nat. Rev. Mol. Cell Biol.* **16**, 651 (2015).
25. X. Gao, J. Wan, B. Liu, M. Ma, B. Shen, S.-B. Qian, Quantitative profiling of initiating ribosomes *in vivo*. *Nat. Methods* **12**, 147–153 (2015).
26. K. Adelman, J. T. Lis, Promoter-proximal pausing of RNA polymerase II: Emerging roles in metazoans. *Nat. Rev. Genet.* **13**, 720–731 (2012).
27. M. Kertesz, Y. Wan, E. Mazor, J. L. Rinn, R. C. Nutter, H. Y. Chang, E. Segal, Genome-wide measurement of RNA secondary structure in yeast. *Nature* **467**, 103–107 (2010).
28. Y. Wan, K. Qu, Q. C. Zhang, R. A. Flynn, O. Manor, Z. Ouyang, J. Zhang, R. C. Spitale, M. P. Snyder, E. Segal, H. Y. Chang, Landscape and variation of RNA secondary structure across the human transcriptome. *Nature* **505**, 706–709 (2014).
29. J. Zhou, J. Wan, X. E. Shu, Y. Mao, X.-M. Liu, X. Yuan, X. Zhang, M. E. Hess, J. C. Bruning, S.-B. Qian, N^6-methyladenosine guides mRNA alternative translation during integrated stress response. *Mol. Cell* **69**, 636–647.e7 (2018).
30. A. B. R. McIntyre, N. S. Gokhale, L. Cerchietti, S. R. Jaffrey, S. M. Horner, C. E. Mason, Limits in the detection of m^{6}A changes using MeRIP/m^{6}A-seq. *Sci. Rep.* **10**, 6590 (2020).
31. K. D. Meyer, DART-seq: An antibody-free method for global m^{6}A detection. *Nat. Methods* **16**, 1275–1280 (2019).
32. Y. Wang, Y. Xiao, S. Dong, Q. Yu, G. Jia, Antibody-free enzyme-assisted chemical approach for detection of N^6-methyladenosine. *Nat. Chem. Biol.* **16**, 896–903 (2020).
33. X. Shu, J. Cao, M. Cheng, S. Xiang, M. Gao, T. Li, X. Ying, F. Wang, Y. Yue, Z. Lu, Q. Dai, X. Cui, L. Ma, Y. Wang, C. He, X. Feng, J. Liu, A metabolic labeling method detects m^{6}A transcriptome-wide at single base resolution. *Nat. Chem. Biol.* **16**, 887–895 (2020).
34. Y. Xiao, Y. Wang, Q. Tang, L. Wei, X. Zhang, G. Jia, An elongation- and ligation-based qPCR amplification method for the radiolabeling-free detection of locus-specific N^6-methyladenosine modification. *Angew. Chem. Int. Ed. Engl.* **57**, 15995–16000 (2018).
35. X. Wang, J. Feng, Y. Xue, Z. Guan, D. Zhang, Z. Liu, Z. Gong, Q. Wang, J. Huang, C. Tang, T. Zou, P. Yin, Structural basis of N^6-adenosine methylation by the METTL3-METTL14 complex. *Nature* **534**, 575–578 (2016).
36. Y. Huang, J. Yan, Q. Li, J. Li, S. Gong, H. Zhou, J. Gan, H. Jiang, G.-F. Jia, C. Luo, C.-G. Yang, Meclofenamic acid selectively inhibits FTO demethylation of m^{6}A over ALKBH5. *Nucleic Acids Res.* **43**, 373–384 (2015).
37. Y. Huang, R. Su, Y. Sheng, L. Dong, Z. Dong, H. Xu, T. Ni, Z. S. Zhang, T. Zhang, C. Li, L. Han, Z. Zhu, F. Lian, J. Wei, Q. Deng, Y. Wang, M. Wunderlich, Z. Gao, G. Pan, D. Zhong, H. Zhou, N. Zhang, J. Gan, H. Jiang, J. C. Mulloy, Z. Qian, J. Chen, C.-G. Yang, Small-molecule targeting of oncogenic FTO demethylase in acute myeloid leukemia. *Cancer Cell* **35**, 677–691.e10 (2019).
38. S. Santagata, M. L. Mendillo, Y. C. Tang, A. Subramanian, C. C. Perley, S. P. Roche, B. Wong, R. Narayan, H. Kwon, M. Koeva, A. Amon, T. R. Golub, J. A. Porco Jr., L. Whitesell, S. Lindquist, Tight coordination of protein translation and HSF1 activation supports the anabolic malignant state. *Science* **341**, 1238303 (2013).
39. J. Wang, A. G. Johnson, C. P. Lapointe, J. Choi, A. Prabhakar, D. H. Chen, A. N. Petrov, J. D. Puglisi, eIF5B gates the transition from translation initiation to elongation. *Nature* **573**, 605–608 (2019).
40. X. Gao, J. Wan, S.-B. Qian, Genome-wide profiling of alternative translation initiation sites. *Methods Mol. Biol.* **1358**, 303–316 (2016).
41. D. Dominissini, S. Moshitch-Moshkovitz, S. Schwartz, M. Salmon-Divon, L. Ungar, S. Osenberg, K. Cesarkas, J. Jacob-Hirsch, N. Amariglio, M. Kupiec, R. Sorek, G. Rechavi, Topology of the human and mouse m6A RNA methylomes revealed by m6A-seq. *Nature* **485**, 201–206 (2012).
42. K. D. Meyer, Y. Saletore, P. Zumbo, O. Elemento, C. E. Mason, S. R. Jaffrey, Comprehensive analysis of mRNA methylation reveals enrichment in 3' UTRs and near stop codons. *Cell* **149**, 1635–1646 (2012).

43. S. Ke, A. Pandya-Jones, Y. Saito, J. J. Fak, C. B. Vågbø, S. Geula, J. H. Hanna, D. L. Black, J. E. Darnell Jr., R. B. Darnell, m^{6}A mRNA modifications are deposited in nascent pre-mRNA and are not required for splicing but do specify cytoplasmic turnover. *Genes Dev.* **31**, 990–1006 (2017).
44. J. Zhou, J. Wan, X. Gao, X. Zhang, S. R. Jaffrey, S.-B. Qian, Dynamic m^{6}A mRNA methylation directs translational control of heat shock response. *Nature* **526**, 591–594 (2015).
45. Y. Li, X. Wang, C. Li, S. Hu, J. Yu, S. Song, Transcriptome-wide N^6-methyladenosine profiling of rice callus and leaf reveals the presence of tissue-specific competitors involved in selective mRNA modification. *RNA Biol.* **11**, 1180–1188 (2014).
46. Y. Wan, K. Tang, D. Zhang, S. Xie, X. Zhu, Z. Wang, Z. Lang, Transcriptome-wide high-throughput deep m^{6}A-seq reveals unique differential m^{6}A methylation patterns between three organs in *Arabidopsis thaliana*. *Genome Biol.* **16**, 272 (2015).
47. M. Chang, H. Lv, W. Zhang, C. Ma, X. He, S. Zhao, Z.-W. Zhang, Y.-X. Zeng, S. Song, Y. Niu, W.-M. Tong, Region-specific RNA m^{6}A methylation represents a new layer of control in the gene regulatory network in the mouse brain. *Open Biol.* **7**, 170166 (2017).
48. Y. Mao, L. Dong, X.-M. Liu, J. Guo, H. Ma, B. Shen, S.-B. Qian, m^{6}A in mRNA coding regions promotes translation via the RNA helicase-containing YTHDC2. *Nat. Commun.* **10**, 5332 (2019).
49. M. P. Mohammad, V. M. Pondelícková, J. Zeman, S. Gunišová, L. S. Valášek, *In vivo* evidence that eIF3 stays bound to ribosomes elongating and terminating on short upstream ORFs to promote reinitiation. *Nucleic Acids Res.* **45**, 2658 (2017).
50. K. D. Meyer, D. P. Patil, J. Zhou, A. Zinoviev, M. A. Skabkin, O. Elemento, T. V. Pestova, S.-B. Qian, S. R. Jaffrey, 5' UTR m^{6}A promotes cap-independent translation. *Cell* **163**, 999–1010 (2015).
51. S. Panneerdoss, V. K. Eedunuri, P. Yadav, S. Timilsina, S. Rajamanickam, S. Viswanadhapalli, N. Abdelfattah, B. C. Onyeagucha, X. Cui, Z. Lai, T. A. Mohammad, Y. K. Gupta, T. H.-M. Huang, Y. Huang, Y. Chen, M. K. Rao, Cross-talk among writers, readers, and erasers of m^{6}A regulates cancer growth and progression. *Sci. Adv.* **4**, eaar8263 (2018).
52. F. McCormick, The potential of targeting Ras proteins in lung cancer. *Expert Opin. Ther. Targets* **19**, 451–454 (2015).
53. M. Ali, E. Kaltenbrun, G. R. Anderson, S. J. Stephens, S. Arena, A. Bardelli, C. M. Counter, K. C. Wood, Codon bias imposes a targetable limitation on *KRAS*-driven therapeutic resistance. *Nat. Commun.* **8**, 15617 (2017).
54. Y. Qiao, B. Zhou, M. Zhang, W. Liu, Z. Han, C. Song, W. Yu, Q. Yang, R. Wang, S. Wang, S. Shi, R. Zhao, J. Chai, J. Chang, A novel inhibitor of the obesity-related protein FTO. *Biochemistry* **55**, 1516–1522 (2016).
55. E. K. Schmidt, G. Clavarino, M. Ceppi, P. Pierre, SUnSET, a nonradioactive method to monitor protein synthesis. *Nat. Methods* **6**, 275–277 (2009).
56. A. R. Gruber, R. Lorenz, S. H. Bernhart, R. Neuböck, I. L. Hofacker, The vienna RNA websuite. *Nucleic Acids Res.* **36**, W70–W74 (2008).
57. S. Rouskin, M. Zubradt, S. Washietl, M. Kellis, J. S. Weissman, Genome-wide probing of RNA structure reveals active unfolding of mRNA structures *in vivo*. *Nature* **505**, 701–705 (2014).
58. D. Dominissini, S. Nachtergaele, S. Moshitch-Moshkovitz, E. Peer, N. Kol, M. S. Ben-Haim, Q. Dai, A. D. Segni, M. Salmon-Divon, W. C. Clark, G. Zheng, T. Pan, O. Solomon, E. Eyal, V. Hershkovitz, D. Han, L. C. Doré, N. Amariglio, G. Rechavi, C. He, The dynamic *N*^{1}-methyladenosine methylome in eukaryotic messenger RNA. *Nature* **530**, 441–446 (2016).
59. G. Bindea, B. Mlecnik, H. Hackl, P. Charoentong, M. Tosolini, A. Kirilovsky, W.-H. Fridman, F. Pagès, Z. Trajanoski, J. Galon, ClueGO: A Cytoscape plug-in to decipher functionally grouped gene ontology and pathway annotation networks. *Bioinformatics* **25**, 1091–1093 (2009).
60. A. Fabregat, S. Jupe, L. Matthews, K. Sidiropoulos, M. Gillespie, P. Garapati, R. Haw, B. Jassal, F. Korninger, B. May, M. Milacic, C. D. Roca, K. Rothfels, C. Sevilla, V. Shamovsky, S. Shorser, T. Varusai, G. Viteri, J. Weiser, G. Wu, L. Stein, H. Hermjakob, P. D'Eustachio, The reactome pathway knowledgebase. *Nucleic Acids Res.* **46**, D649–D655 (2018).

Acknowledgments: We would like to thank C. M. Counter (Duke University Medical Center) for providing the inducible RAS^{G12V} system. We also thank C.-G. Yang (Shanghai Institute of Materia Medica, Chinese Academy of Sciences) for providing the compound FB23-2. We are grateful to Cornell University Life Sciences Core Laboratory Center for sequencing support. **Funding:** This work was supported, in part, by grants from the U.S. National Institutes of Health (R21CA227917) and HHMI Faculty Scholar (55108556) to S.-B.Q. **Author contributions:** S.-B.Q. conceived the project and designed the experiments. L.D. performed most of the experiments, and Y.M. conducted most of the data analysis. A.Z. conducted tumorigenesis using the orthotopic mouse model. X.-M.L. and J.Z. contributed to the m^{6}A-seq, and J.W. assisted with the initial data analysis. All authors discussed the results and edited the manuscript. S.-B.Q. wrote the manuscript. **Competing interests:** The authors declare that they have no competing interests. **Data and materials availability:** All data needed to evaluate the conclusions in the paper are present in the paper and/or the Supplementary Materials. RNA-seq, Ribo-seq, QTI-seq, and m^{6}A-seq data are available on the GEO database with GEO number GSE159210.

Submitted 6 July 2020
Accepted 30 December 2020
Published 17 February 2021
10.1126/sciadv.abd6927

Citation: L. Dong, Y. Mao, A. Zhou, X.-M. Liu, J. Zhou, J. Wan, S.-B. Qian, Relaxed initiation pausing of ribosomes drives oncogenic translation. *Sci. Adv.* **7**, eabd6927 (2021).

Science Advances

Relaxed initiation pausing of ribosomes drives oncogenic translation

Leiming Dong, Yuanhui Mao, Aidong Zhou, Xiao-Min Liu, Jun Zhou, Ji Wan and Shu-Bing Qian

Sci Adv **7** (8), eabd6927.
DOI: 10.1126/sciadv.abd6927